




PixRO: Pixel-Distributed Rotational Odometry with Gaussian Belief Propagation

Ignacio Alzugaray^{1,2}, Riku Murai², and Andrew Davison^{1,2}

¹ Dyson Robotics Lab, Imperial College London, UK

² Department of Computing, Imperial College London, UK
{i.alzugaray,riku.murai15,a.davison}@imperial.ac.uk

Abstract. Visual sensors are not only becoming better at capturing high-quality images but also they have steadily increased their capabilities in processing data on their own on-chip. Yet the majority of Visual Odometry (VO) pipelines rely on the transmission and processing of full images in a centralized unit (*e.g.* CPU or GPU), which often contain much redundant and low-quality information for the task. In this paper, we address the task of frame-to-frame rotational estimation but, instead of reasoning about relative motion between frames using the full images, distribute the estimation at pixel-level. In this paradigm, each pixel produces an estimate of the global motion by only relying on local information and local message-passing with neighbouring pixels. The resulting per-pixel estimates can be then communicated to downstream tasks, yielding higher-level, informative cues instead of the original raw pixel-readings. We evaluate the proposed approach on real public datasets, where we offer detailed insights about this novel technique and open-source our implementation for the future benefit of the community.

Keywords: Rotation Estimation · Pixel processing · Gaussian Belief Propagation · Distributed Optimization

1 Introduction

In recent years, cameras have evolved not only to capture high-quality images but to pre-process the data they capture at pixel- or image-level, applying low-level algorithms such as gamma correction or noise suppression. The design of novel vision-based algorithms, however, has largely disregarded the increasing computational capacity of visual sensors and their pixels. In most high-level vision tasks such as, for instance, VO, all individual pixel readings are transmitted from the sensor to an external processing unit such as a CPU or a GPU. In these units, the data is batch-processed as an image to jointly reason about relative camera motion in a centralized manner since individual pixel readings are often noisy or poorly informative. Nonetheless, this shows that transmitting these individual pixel readings and combining their information in an off-sensor processor is an inefficient step as only a small fraction of these readings offer non-redundant, high-quality information for most high-level tasks in a vision-based pipeline.

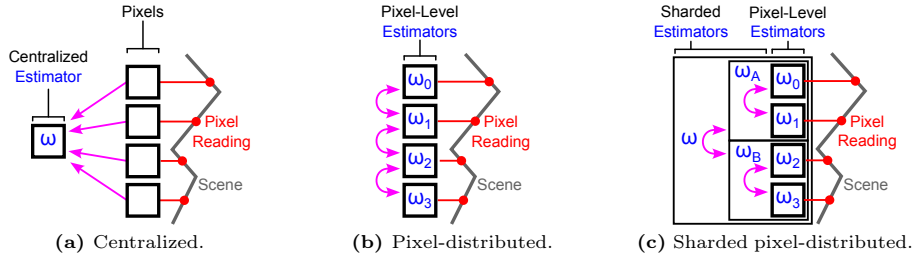


Fig. 1: Types of camera motion estimation architecture based on the locus of computation. In a centralized set-up (left), individual pixel readings (red) of the scene (gray) are communicated (magenta) to a centralized processing unit to estimate global relative motion (blue). In a pixel-distributed architecture (right), each pixel only communicates with its local neighbourhood to achieve a consensus of the global motion replicated at each pixel. In a sharded pixel-distributed configuration (right), individual pixel-level estimators are clustered in groups that only communicate their motion estimate to other so-called sharded estimators in a hierarchical manner, avoiding the need to transmit information about individual raw pixel readings upstream.

Our paper aims to explore the research space for hardware-aware algorithms and, in particular, pixel-distributed VO in light of the increasing computational capability at the pixel level in emerging visual sensors such as SCAMP-5 [15]. We particularly address the task of frame-to-frame rotation estimation, a subproblem within VO traditionally tackled using full images in a centralized manner (Fig. 1a). Instead, here we propose an approach to distribute the estimation at the pixel level without the need for centralized processing. In our algorithm, each pixel is assumed to have a certain computational capability, and is able to independently estimate the global rotation by only using local message-passing communication with other neighbouring pixels (Fig. 1b). We develop our approach using Gaussian Belief Propagation (GBP), a traditional technique [8, 16] that has seen a notable resurgence in the past years [38, 39, 42, 44, 50], that presents a flexible and efficient framework for distributed optimization. The pixel-distributed algorithm presented in this paper defines an interesting and promising paradigm shift on which vision-based pipelines could directly rely on high-level motion estimates directly synthesized within each sensor device (Fig. 1c).

In summary, the contributions of this paper are:

- A novel vision-based frame-to-frame rotation estimation algorithm that, to the best of our knowledge, is the first that can be distributed at pixel-level using only local message-passing.
- An explicit and complete description of the GBP framework applied to 3D rotations with additional insights for real-world deployment.
- An extensive evaluation of different proposed variants against established baselines on public datasets using real-world data and an in-depth analysis of the characteristics of the method.

2 Related work

As the field of VO and Visual Simultaneous Localization and Mapping (VSLAM) reaches maturity [13, 17, 20, 21, 32, 34, 37, 49], many established systems have been effectively migrated to hardware accelerators, offloading either the visual front-end [23, 54], back-end [9, 48] or even the entire pipeline [4, 53]. More aligned with our paper, direct visual frame-to-frame rotation estimation is more closely related to optical flow estimation [6] and direct image alignment [5, 35], which have also been extensively explored for hardware acceleration [11, 30, 55]. Most of these adaptations, however, largely parallelize the computation of resource-intensive subtasks within each method while the joint estimation still occurs in a centralized manner within a specialized hardware architecture.

Only a handful of papers, however, have addressed motion estimation using the near-sensor processing capabilities emerging in novel sensors such as SCAMP-5 [14]. For instance, in [40], visual features are directly extracted by a pixel processor while their processing for VO is offloaded to a CPU. In [10] visual data is directly processed on pixel-processors into edges that are tracked to perform image alignment via image shifting, scaling and rotation, similar to [2, 3]. While only 4-Degrees of Freedom (DoF) VO is achieved in [10], the approach is extended to 6-DoF VO in [36] by fusing information from an Inertial Measurement Unit (IMU). The work described in [25] explores a similar image alignment technique to perform VO against the ground-plane using near-sensor processing. These approaches’ algorithmic designs, however, are primarily guided by the limitations of the physical sensor itself (e.g., the lack of arithmetic operations such as multiplication) which overly restrict the search space for the algorithmic design of near-sensor motion estimation. In this paper, we design our algorithm backwards, by investigating what could be the best technique to directly estimate global motion at pixel level so that our insights can guide the design of new emerging hardware.

Distributed rotation estimation has been extensively studied for multiple images in the context of rotation averaging or Bundle Adjustment (BA) [22, 24, 27, 52, 57]. These distributed approaches, however, reason about relative rotations considering the images as an individual entity, often employing direct relative measurements or groups of visual features. In this paper, however, we further decompose the distributed estimation process to the most fundamental elements, *i.e.* the pixels, and employ only direct pixel readings.

Among various distributed optimization frameworks [26], Alternating Direction Method of Multipliers (ADMM) [12] has gained notable momentum and has been successfully applied to VO and VSLAM tasks [22, 57, 58]. Nonetheless, traditional techniques such as GBP [8, 16] have seen a reemergence due to their appealing probabilistic interpretation, asynchronicity and low-computational requirements. GBP has been successfully applied to distributed tasks such multi-agent localization [38, 39] or bundle-adjustment on a graph-processor [44]. Closest to our work is [50] which performs pixel-wise VO using GBP, however, requires depth and random non-local connectivity. [42] uses GBP and event camera for optical flow estimation, but unlike ours, cannot directly predict the motion of

the camera. In this paper, to the best of our knowledge, we explore for the first time the application of GBP to frame-to-frame rotation estimation distributed at pixel level.

3 Methodology

3.1 Gaussian Factor Graph

Gaussian Factor graphs [18] are bipartite graphs $\mathcal{G} = \{\mathcal{V}, \mathcal{F}\}$ that model probabilistic relationships between Gaussian distributed variables $\mathbf{v} \in \mathcal{V}$ and Gaussian distributed factors $f \in \mathcal{F}$. Here, we represent Gaussian distributions in standard form $\mathcal{N}(\boldsymbol{\mu}, \Sigma)$, with mean $\boldsymbol{\mu}$ and covariance Σ , or in canonical form $\mathcal{N}^{-1}(\boldsymbol{\eta}, \Lambda)$ with information vector $\boldsymbol{\eta} = \Lambda^{-1}\boldsymbol{\mu}$ and precision matrix $\Lambda = \Sigma^{-1}$. Individual factors f_i model probabilistic constraints over a subset of variables $\mathbf{v}_{f_i} = \mathfrak{N}(f_i) \subseteq \mathcal{V}$ according to the factor potential $f_i(\mathbf{v}_{f_i}) \propto \exp(-E_{f_i}(\mathbf{v}_{f_i}))$, modelled with an inducing energy term [33] evaluated on the variables' mean $\boldsymbol{\mu}_{\mathbf{v}}$, i.e. $E(\mathbf{v}) = E(\boldsymbol{\mu}_{\mathbf{v}})$. These factors essentially shape the likelihood of any provided configuration \mathcal{V} as $p(\mathcal{V}) = \prod_i f_i(\mathbf{v}_{f_i})$ given a set of independent observations, enabling Maximum Likelihood Estimation (MLE) as in:

$$\mathcal{V} = \arg \min_{\mathcal{V}} -\log p(\mathcal{V}) = \arg \min_{\mathcal{V}} \sum_{f_i \in \mathcal{F}} E_{f_i}(\mathbf{v}_{f_i}). \quad (1)$$

The energy induced by each factor is characterized by a residual function \mathbf{r} as $E(\boldsymbol{\mu}) = \frac{1}{2}\|\mathbf{r}(\boldsymbol{\mu})\|_{\Lambda_r}^2$, with $\|\mathbf{r}\|_{\Lambda}^2 = \mathbf{r}^T \Lambda \mathbf{r}$, that is zero-centered Gaussian-distributed $\mathbf{r} \sim \mathcal{N}^{-1}(\mathbf{0}, \Lambda_r)$.

3.2 Incremental Gaussian Belief Propagation in $\mathbb{S}\mathbb{O}(3)$

While Eq. (1) is often addressed by techniques such as Gauss-Newton or gradient descent, GBP offers a simple paradigm to MLE by locally passing Gaussian messages among factors and variables to compute the marginals of the joint distribution. These message-passing steps are efficient as they have closed-form expressions under Gaussian assumption and can be applied independently at each node and factor without explicit synchronization. This makes GBP an ideal candidate for efficient distributed inference while providing an explicit probabilistic interpretation of the problem. Here we briefly summarize the key steps and refer the reader to previous work on the topic for further details [8, 16, 38, 39, 43, 47].

In particular, the scope of our paper is focused on distributed rotation estimation and thus all the variables $\mathbf{v} \in \mathcal{V}$ in our graph represent rotations in $\mathbb{S}\mathbb{O}(3)$. This generally establishes non-linear relationships on the factors operating on such variables with respect to their underlying minimal representation, imposing the need for finding the solution of MLE problem incrementally. Following [39], we extend GBP to handle Lie groups. Let $\bar{\boldsymbol{\mu}} \in \mathbb{S}\mathbb{O}(3)$ be the linearization point for a given rotation variable, *i.e.* its mean. We define a random variable as:

$$\mathbf{v} = \bar{\boldsymbol{\mu}} \oplus \bar{\boldsymbol{\mu}} \xi, \text{ where } \bar{\boldsymbol{\mu}} \xi \sim \mathcal{N}(0, \Sigma_{\mathbf{v}}) \quad (2)$$

By defining \mathbf{v} through the random variable $\bar{\mu}\xi \in \mathfrak{so}(3)$, since Lie algebra is isomorphic to vector space, all the commonly used probabilistic methodologies can be reused [7, 51]. Notations and operations from [51] are leveraged for the rest of the paper for $\mathbb{SO}(3)$; for example, \oplus applies exponential map and composition in one operation.

The residual of any factor involving such a variable can be approximated around such a linearization point using a Taylor expansion as:

$$\mathbf{r}(\boldsymbol{\mu}) = \mathbf{r}(\bar{\boldsymbol{\mu}} \oplus \boldsymbol{\tau}) \approx \mathbf{r}(\bar{\boldsymbol{\mu}}) + \left. \frac{D\mathbf{r}}{D\boldsymbol{\mu}} \right|_{\boldsymbol{\mu}=\bar{\boldsymbol{\mu}}} \boldsymbol{\tau} = \mathbf{r}(\bar{\boldsymbol{\mu}}) + \mathbf{J}(\bar{\boldsymbol{\mu}})\boldsymbol{\tau} = \bar{\mathbf{r}} + \bar{\mathbf{J}}\boldsymbol{\tau}, \quad (3)$$

and each energy term can be approximated into an incremental form as:

$$E(\boldsymbol{\tau}) = \frac{1}{2} \|\mathbf{r}(\bar{\boldsymbol{\mu}} \oplus \boldsymbol{\tau})\|_{\Lambda_r}^2 \approx \frac{1}{2} \|\bar{\mathbf{r}} + \bar{\mathbf{J}}\boldsymbol{\tau}\|_{\Lambda_r}^2 \propto \frac{1}{2} \boldsymbol{\tau}^T \bar{\mathbf{J}}^T \Lambda_r \bar{\mathbf{J}} \boldsymbol{\tau} + (\bar{\mathbf{J}}^T \Lambda_r \bar{\mathbf{r}})^T \boldsymbol{\tau}, \quad (4)$$

which, in turn, transforms the original factor potential f_i for the residual \mathbf{r}_i into the incremental, linearized form $\bar{\mu}f_i \sim \mathcal{N}^{-1}(\bar{\boldsymbol{\eta}}_{f_i}, \bar{\Lambda}_{f_i})$, with $\bar{\boldsymbol{\eta}}_{f_i} = -\bar{\mathbf{J}}_i^T \Lambda_{r_i} \bar{\mathbf{r}}_i$ and $\bar{\Lambda}_{f_i} = \bar{\mathbf{J}}_i^T \Lambda_{r_i} \bar{\mathbf{J}}_i$, around the linearization point $\bar{\boldsymbol{\mu}}$.

Adopting these incremental forms and $\mathbb{SO}(3)$ in the GBP framework, we define the following operation to keep the notation concise:

$$\mathbf{G} = \bar{\boldsymbol{\mu}} \boxplus \bar{\mu} \mathbf{g} = \bar{\boldsymbol{\mu}} \boxplus \mathcal{N}(\bar{\mu} \boldsymbol{\tau}, \bar{\mu} \Sigma) = (\bar{\boldsymbol{\mu}} \oplus \bar{\mu} \boldsymbol{\tau}) \oplus \mathcal{N}(0, \mathbf{J}_r(\bar{\mu} \boldsymbol{\tau}) \bar{\mu} \Sigma \mathbf{J}_r^T(\bar{\mu} \boldsymbol{\tau})), \quad (5)$$

$$\bar{\mu} \mathbf{g} = \mathbf{G} \boxminus \bar{\boldsymbol{\mu}} = (\mathbf{G} \bar{\boldsymbol{\mu}} \oplus \mathcal{N}(0, \mathbf{G} \Sigma)) \boxminus \bar{\boldsymbol{\mu}} = \mathcal{N}(\boldsymbol{\theta}, \mathbf{J}_r^{-1}(\boldsymbol{\theta}) \mathbf{G} \Sigma \mathbf{J}_r^T(\boldsymbol{\theta})), \quad (6)$$

where $\boldsymbol{\theta} = \mathbf{G} \bar{\boldsymbol{\mu}} \ominus \bar{\boldsymbol{\mu}}$ and $\mathbf{J}_r(\mathbf{x})$ is the right-jacobian $\mathbb{SO}(3)$ [51].

In the following lines, we describe the main GBP steps adapted to this incremental $\mathbb{SO}(3)$ estimation. Note that individual nodes and factors might operate on different linearization points, and thus their transformation is crucial in integrating the exchanged information via message-passing. All the messages are Gaussian and are parameterized as Eq. (2), using a $\mathbb{SO}(3)$ element and an associated uncertainty defined in its tangent space.

Factor-to-Variable messages: Each factor $f_j \in \mathcal{F}$ is evaluated at linearization point $\bar{\boldsymbol{\mu}}$ obtained from the means of the its connected variables $\mathbf{v}_i \in \mathfrak{N}(f_j) \subseteq \mathcal{V}$ to produce an incremental factor potential $\bar{\mu}f_j$. This is combined with the incoming variable-to-factor messages $\mathbf{m}_{\mathbf{v}_k! f_j}$ at their linearization points $\bar{\boldsymbol{\mu}}_k$ to produce the local outgoing factor-to-variable messages:

$$\mathbf{m}_{f_j! \mathbf{v}_i} = \bar{\boldsymbol{\mu}}_i \boxplus \left(\sum_{\mathbf{v}_2 \in \mathfrak{N}(f_j)/\mathbf{v}_i} \bar{\mu} f_j(\mathbf{v}) \prod_{\mathbf{v}_k \in \mathfrak{N}(f_k)/\mathbf{v}_i} (\mathbf{m}_{\mathbf{v}_k! f_j} \boxminus \bar{\boldsymbol{\mu}}_k) \right). \quad (7)$$

The outgoing message is computed by marginalization, then retraction onto $\mathbb{SO}(3)$ around the outgoing variable's linearization point $\bar{\boldsymbol{\mu}}_i$.

Variable-to-Factor messages: each variable $\mathbf{v}_i \in \mathcal{V}$ send message to each of factors it is connected to $f_j \in \mathfrak{N}(\mathbf{v}_i) \subseteq \mathcal{F}$ by leveraging its own mean as a

linearization point $\bar{\boldsymbol{\mu}}_i$:

$$\mathbf{m}_{\mathbf{v}_i!} f_j = \bar{\boldsymbol{\mu}}_i \boxplus \left(\prod_{f \in \mathfrak{N}(\mathbf{v}_i)/f_j} (\mathbf{m}_{f!} \mathbf{v}_i \boxminus \bar{\boldsymbol{\mu}}_i) \right). \quad (8)$$

Variable belief update: Similarly, the marginal posteriors of each variable, *i.e.* that best explain the constraints imposed by the factors, are computed by merging the incoming factor-to-variable messages in the local space:

$$\mathbf{v}_i = \bar{\boldsymbol{\mu}}_i \boxplus \left(\prod_{f \in \mathfrak{N}(\mathbf{v}_i)} (\mathbf{m}_{f!} \mathbf{v}_i \boxminus \bar{\boldsymbol{\mu}}_i) \right) \quad (9)$$

$$(10)$$

Among these three steps, this last operation is the only one that modifies the linearization point of the problem by changing the \mathbf{v}_i as its mean is modified.

Note that although GBP lacks convergence guarantees for generic “loopy” graphs with cycles, it has been empirically demonstrated to produce compelling results for a variety of applications [19, 29, 41].

3.3 Centralized Frame-to-Frame Direct Rotation Estimation

In general terms, our goal is to find the rotation, denoted by the $\boldsymbol{\mu} \in \mathbb{S}\mathbb{O}(3)$, that best describes the relative rotation between two image frames \mathcal{I}_r and \mathcal{I}_l captured from the same static scene using a calibrated camera under pure-rotational motion. These images are assumed to be distortion-free and grayscale. We can geometrically map individual pixel locations \mathbf{p} from image \mathcal{I}_l onto image \mathcal{I}_r using the warping function:

$$\mathcal{W}(\mathbf{p}; \boldsymbol{\mu}) = \pi \left(\mathbf{K} \boldsymbol{\mu} \mathbf{K}^{-1} [\mathbf{p}; 1]^T \right), \quad (11)$$

where \mathbf{K} is the camera’s intrinsic matrix, and $\pi(\mathbf{P}) = [p_x/p_z, p_y/p_z]^T$ is the projection function. We pose the problem as direct image-alignment optimization between the warped image \mathcal{I}_l and image \mathcal{I}_r over the whole image domain Ω :

$$\boldsymbol{\mu} = \arg \min_{\boldsymbol{\mu}} \sum_{\mathbf{p} \in \Omega} \|\mathcal{I}_l[\mathbf{p}] - \mathcal{I}_r[\mathcal{W}(\mathbf{p}; \boldsymbol{\mu})]\|^2. \quad (12)$$

Solving this optimization with traditional iterative Non-Linear Least Squares (NLLS) implies the transmission of all individual pixel residuals and their Jacobians to a central processing unit that iteratively yields the best global rotation estimation. For these reasons, this method is referred to as a *centralized* and used as the main baseline in our evaluation.

Note that Eq. (12) represents the simplest form of direct-image alignment and, thus, can only handle small camera rotations due to its small convergence basin, which will be reflected in our evaluations. While more advanced techniques could be applied, such as multiscale pyramid [5], we opt here to focus on this bare-bones version of the problem so that we can analyse better the characteristics of the proposed method without additional layers of complexity.

3.4 Distributed Frame-to-Frame Direct Rotation Estimation

In this section, we transform the centralized formulation described in Eq. (12) into a pixel-level distributed problem for which we aim to single estimate of the global rotation $\boldsymbol{\mu}_i$ at each pixel \mathbf{p}_i , instead of a centralized estimate. These per-pixel estimates $\boldsymbol{\mu}_i$ are the mean of the per-pixel variables \mathbf{v}_i as defined in Sec. 3.1, which we will iteratively solve for using GBP as described in Sec. 3.2. Each of the per-pixel variables is fully constrained by factors, which are described in the following sections (see Fig. 2a).

Photometric Data Factor This factor essentially mirrors the original formulation from Eq. (12) at pixel level and indicates the photometric difference between individual pixel readings across the two considered images as in

$$E_D^i(\boldsymbol{\mu}_i) = \frac{1}{2} \|\mathcal{I}_l[\mathbf{p}_i] - \mathcal{I}_r[\mathcal{W}(\mathbf{p}_i; \boldsymbol{\mu}_i)]\|_{\Lambda_D}^2, \quad (13)$$

where each pixel is assumed to be aware of its location with respect to the camera center and the camera intrinsic \mathbf{K} so that \mathcal{W} can be applied. In this paper, we assume that each pixel can have access to the photometric information of other pixels in the array (which could be implemented using routing mechanisms).

It is crucial to note that, by breaking down the original problem into individual per-pixel photometric residuals applied on grayscale images, this factor only imposes rank-deficient constraints onto the rotation estimate $\boldsymbol{\mu}_i$. Consequently, other factors are required to fully constrain the problem, such as the prior and regularization terms detailed next.

Prior Factor This factor directly constraint the per-pixel estimated rotation through an educated guess $\hat{\boldsymbol{\mu}}_i$,

$$E_P^i(\boldsymbol{\mu}_i) = \frac{1}{2} \|\boldsymbol{\mu}_i \ominus \hat{\boldsymbol{\mu}}_i\|_{\Lambda_P}^2, \quad (14)$$

where \ominus represents distance metric of choice for comparing rotations [28, 45, 46]. In our implementation, we choose the geodesic distance metric and use the previously known mean of the variable as the guess, *i.e.* its linearization point $\hat{\boldsymbol{\mu}}_i = \bar{\boldsymbol{\mu}}_i$. This way, this factor only applies local constraint on the incremental step update of a variable, similar to a trust-region in traditional NLLS for the GBP framework described in Sec. 3.2. While this factor might slow down the overall convergence of the system, it also stabilizes it in the presence of noise of highly irregular local gradients from Eq. (13).

Regularization Factor In our algorithm, individual pixel variables exchange information with other pixels to jointly reason about the global motion, which is represented by a regularization term:

$$E_R^i(\boldsymbol{\mu}_i) = \sum_{\mathbf{v}_j \in \mathfrak{N}_R(\mathbf{v}_i)} \frac{1}{2} \|\boldsymbol{\mu}_j \ominus \boldsymbol{\mu}_i\|_{\Lambda_R}^2, \quad (15)$$

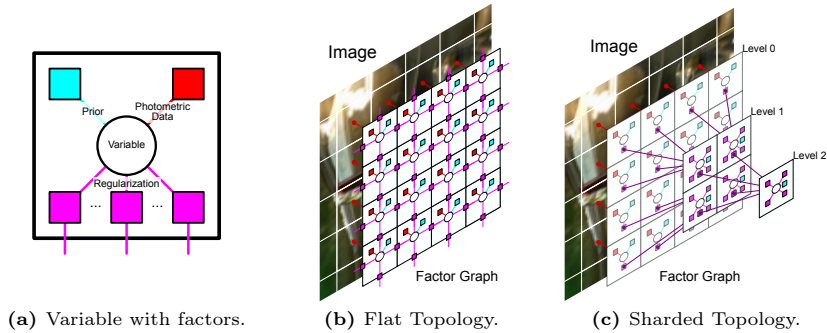


Fig. 2: Examples of graph topologies explored in this paper for the frame-to-frame rotation estimation. Each variable (white) can consider a photometric data factor (red), connected to the sensor image, and always includes prior (cyan) and regularization factor(magenta) that determines the topology.

where $\mathfrak{N}_R(\mathbf{v}_i)$ identifies the set of other neighbouring, connected pixel variables in the graph. By enforcing locally connected pixels to yield the same global rotation (as they belong to the same sensor), this factor essentially propagates information across the pixels and achieves global consensus of the frame-to-frame rotation estimate upon convergence.

While the photometric factor is the main driver for our rotational estimation, it tends to be extremely unreliable at the pixel level, either due to spurious noise, small convergence basins or simply because an individual pixel is observing an uninformative textureless area in the majority of the cases. In such situations, the regularization factor plays a fundamental role in the accurate estimation of the global rotation. Yet a careful balance between photometric and regularization must be achieved to not completely disregard the image data while achieving a global consensus as we analyse in Sec. 5. Given the importance of regularization in our approach, we discuss different topology patterns for connecting variables in the following section.

3.5 Graph Topology

Based on the presented framework, we explore two different configurations with distinctive graph topologies, leading to important performance differences as explored in Sec. 5. Note that, in this paper, we are making use of a fixed, pre-determined graph topology with only local connectivity to simulate typical constraints that a pixel-processor would exhibit, whereas, in practice, the GBP solver that acts upon this graph would allow us to mutate these connections on-the-fly, fostering future research.

Flat Topology (Fig. 1b and Fig. 2b): In this simple configuration, pixels are only connected to their immediate vertical and horizontal neighbouring pixels

via regularization factors. Added to their photometric and prior factors, each pixel variable is connected to up to 6 factors in the factor graph (see Sec. 3.1).

Sharded Topology (Fig. 1c and Fig. 2c): In this configuration, we consider two types of variables, photometric and sharded. Photometric variables have access to raw pixel readings from the images and thus have associated photometric factors. Sharded variables are auxiliary variables that act as a bridge between other photometric and/or sharded variables but do not have associated photometric factors. Instead, non-overlapping groups of 2×2 photometric variables are all connected to a single sharded variable in the next level via regularization factors. In this new level of only sharded variables, non-overlapping groups of 2×2 are connected to the next level via regularization factors. This process is repeated until a single sharded “apex” variable remains, at the top of the pyramid structure. Both photometric and sharded variables make use of prior factors. The motivation behind this topology is that it creates shorter paths to propagate information between distant pixels, enabling faster convergence. Moreover, the resulting topology is a tree in which the GBP estimation process is better behaved without loopy behaviour [41], in contrast to the *flat* topology. Lastly, using this configuration raw image information never leaves the photometric variables as sharded variables only consider rotation estimates, which is not only ideal for privacy-preserving applications but also makes it interesting for the fusion of estimates from independent sensors, which we leave for future research.

4 Implementation details

In contrast to most publicly available GBP implementations in the literature [16, 43], here we do not explicitly consider three different steps of Eqs. (7) to (9) to be synchronously interleaved for factors and nodes. Instead, we sequentially interleave only two steps: the updating of all of the factor-to-variable messages (Eq. (8)) and the update of all variable beliefs whereas variable-to-factor messages (Eq. (7)) are computed on-demand. As both steps occur sequentially, we store the factor-to-variable messages in a local frame given a linearization point and also update them as soon as the linearization point changes, *i.e.* just after a variable belief update, using Eqs. (5) and (6).

While the presented algorithm is designed to harness the increasing computational capabilities of pixels in smart visual sensors, this paper presents a proof of concept of such a technique to explore its capabilities and limitations. As such, we deploy such an algorithm in a desktop machine and fully parallelize each of the GBP steps previously described using PyTorch-CUDA.

5 Experimental Evaluation

5.1 Data Generation

For the proposed experiments, we generate our data from a public dataset of panoramic 360 images, Pano3D GibsonV2 [1, 56], obtained from the projection

of 3D scans in the real-world. On each run, poses are generated by randomly selecting two rotations around the same camera center, as discussed in Sec. 3.3, limited to rotations of 1 between these frames. We synthesize the images from each pose by projecting equirectangular images with a distortion-free, projective camera model of 60 field-of-view and a resolution of 128x128px.

Our evaluation mainly explores the characteristics of the proposed pixel-distributed visual rotation estimation method, emphasizing and analyzing the capabilities and limitations of the *flat* and *sharded* configurations (Sec. 3.5). As a baseline, we additionally consider a traditional *centralized* configuration, where the NLLS problem in Eq. (12) is optimized using a simple gradient descent. Note that this *centralized* configuration is expected to perform more effectively than the proposed distributed ones, as each optimization step has direct access to information from all the pixels to yield the best estimate. As such, the *centralized* baseline is only included for reference, whereas we focus our evaluation on the details of how to distribute the problem at pixel level.

In the following experiments, we report the normalized average rotational error as our main metric. Unless otherwise specified, this is computed as the average geodesic distance between all individual rotation estimates at each variable and the ground-truth frame-to-frame global rotation, normalized with respect to the magnitude of such a rotation. To overcome spurious effects, the reported metrics are collated from a collection of up to 50 different runs for each experiment, providing a more statistically meaningful result. In our evaluation, we will consider modelling factors from Sec. 3.4 with isotropic noise so that $\Lambda_i = \Sigma_i^{-1} = \sigma_i^{-2}\mathbf{I}$, and specifying σ_P , σ_D and σ_R , for prior (Eq. (14)), photometric data (Eq. (13)), and regularization (Eq. (15)) terms.

5.2 Performance of Pixel-Distributed Rotation Estimation

In this experiment, we present a head-to-head comparison of all considered configurations: *flat*, *sharded*, and *centralized*. For fairness, we experimentally establish the best set of parameters for both configurations, employing $\{\sigma_P, \sigma_D, \sigma_R\} = \{10^{-2}, 10^{-1}, 10^{-2}\}$ for the *flat* topology and $\{\sigma_P, \sigma_D, \sigma_R\} = \{10^{-2}, 10^{-1}, 10^{-4}\}$ for the *sharded* topology. Factor noise is often modelled according to experimental residual evaluation, which should be independent of the underlying topology. However, in this case, the topologies present notably different behaviour for the same parameters, as we will show in the following experiments. The chosen parameters strike a good balance between accuracy, convergence and stability for the distributed configurations.

From the results presented in Fig. 3, we observe that the *sharded* topology performs generally better than the *flat* topology. The former is able to more effectively converge and achieve rapid consensus of the global estimate. Information from distant pixels can be propagated in fewer iterations via the hierarchical topology of *sharded* in comparison to the *flat* communication pattern. Moreover, the *sharded* topology offers a much better estimate of the global rotation at each variable in a reasonable number of iterations, performing comparably

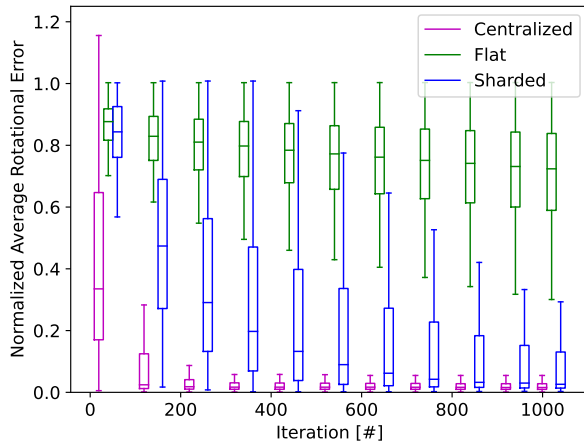


Fig. 3: Progression of the error with respect to the number of optimization steps for the *centralized* configurations or GBP iterations for the distributed ones, *flat* and *sharded*.

to the *centralized* upon convergence. On the other hand, the *flat* topology often struggles to converge to a meaningful estimate, as consensus is usually not achieved. As expected, the pixel-distributed approaches underperform with respect to the *centralized* approach, in both convergence rate and final accuracy, as all information is jointly used at each iteration to yield the best estimate. Nonetheless, we believe that the distributed approaches offer an interesting and yet unexplored alternative to rotation estimation at a pixel level, further relaxing assumptions on the processing of the pixel information and potentially leading to new research avenues at the intersection between hardware and software.

5.3 Interactions between photometric data and regularization

This section focuses on a comparison between the *flat* and *sharded* topologies, offering multiple insights by diving into the internals of the proposed framework. This analysis is not only important to understand better the performance gap between the presented topologies, as evidenced in the previous experiment, but also identifies key aspects and potential improvements for other future approaches to be built within our estimation framework.

As discussed in Sec. 3.4, the per-pixel inference is mainly driven by the photometric data error. Yet, regularization is necessary as it is the only means to communicate information across individual variables and achieve global consensus on the rotation estimates. In this experiment we explore the fine balance between these two aspects by fixing $\{\sigma_P, \sigma_D\} = \{10^{-2}, 10^{-1}\}$ and varying the strength of the regularization: $\sigma_R = 10^{-4}$ (High), $\sigma_R = 10^{-3}$ (Mid), and $\sigma_R = 10^{-2}$ (Low). The results for both *flat* and *sharded* topologies are presented in Fig. 4.

Employing a *flat* topology, we observe in Fig. 4a that strong regularization halts the problem around the initial estimate, leading to non-meaningful esti-

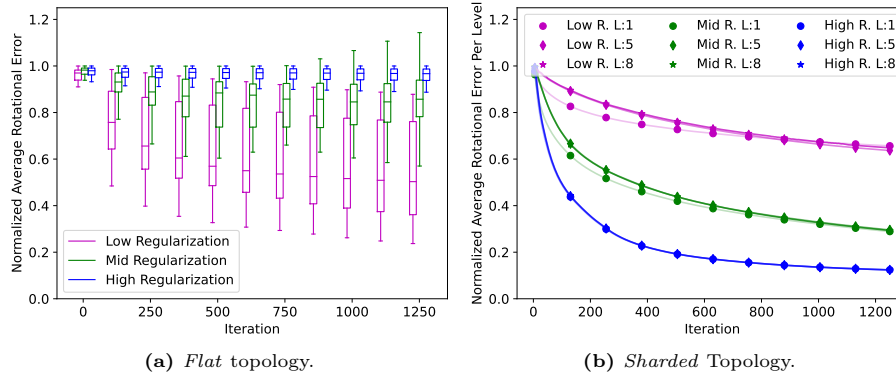


Fig. 4: Balance between photometric data and different strengths of regularization.

mates regardless of the number of iterations. Alternatively, using weak regularization, some of individual variables yield a reasonable estimate of the global rotation. However, they effectively ignore the information from neighbouring variables and thus cannot achieve global consensus at convergence, leading to overall inaccurate estimation. More interestingly, intermediate regularization strength can lead to instability of the system and, in some cases, divergence. This is the result of poor variable estimates incorrectly receiving positive feedback from neighbours in the “loopy” graph; we will analyse this later.

Fig. 4b offers equivalent analysis for the *sharded* topology. Here we opt to leverage the hierarchical structure of this topology and report the rotational error summarized across individual levels, from the lowest with only photometric variables, to the top level, with only one apex variable (see Sec. 3.5). For clarity, we show only three (L:1, L:5, L:8) of the eight levels, and only show the means, as the statistical trends match those depicted in Fig. 3. Results indicate that rotation estimation accuracy at higher levels lags with respect to the variables closer to the photometric data in early iterations. This is because higher-level variables mix conflicting estimates from different parts of the image, achieving consensus only after a few more iterations. In the presence of strong regularization, however, this discrepancy is barely noticeable and all the individual estimates evolve jointly, making the system behave like a *centralized* approach despite using only local message-passing communication.

5.4 Stability analysis on graphs with loops

Our previous results indicate a noticeable difference in response to strong regularization between *flat* and *sharded* topologies. In the former case, estimation achieves consensus but to an incorrectly estimated global rotation near initialization, whereas the latter achieves its best-performing configuration. In this section, we investigate the root cause for this difference, which can be explained by the fact that *flat* topology creates a graph with multiple loops whereas the

sharded topology is essentially a tree. Estimates from GBP become more overconfident the “loopier” the factor graph is, which is a well-known effect described in the literature [29,41]. To evidence this issue, Fig. 5a indicates the average variable uncertainty for each of the topologies, measured as the Frobenius norm of their covariance. In this analysis, we again explore three different degrees of regularization as in Sec. 5.3. We observe that, for the same set of parameters, the *flat* topology consistently yields overall lower uncertainty in the variables compared to the *sharded* topology. Note that this holds even when the *flat* topology has fewer factors that constrain the graph when compared to the *sharded* topology.

The overconfidence in variable estimates due to graph loops may lead to positive feedback of poorly estimated variables, causing unstable behaviour as depicted in Fig. 4a. While keeping the same set of parameters, $\{\sigma_D, \sigma_R\} = \{10^{-1}, 10^{-3}\}$, we can mitigate the instability of the system by strengthening the prior $\sigma_P = \{10^{-1}, 10^{-2}, 10^{-3}, 10^{-4}\}$ applied at each GBP update, as represented in Sec. 5.4, at the expenses of a lower convergence rate. We identify this stabilizing effect related to the prior to be closely related to other techniques applied to GBP such as messaging damping [38,39] or diagonal loading [31].

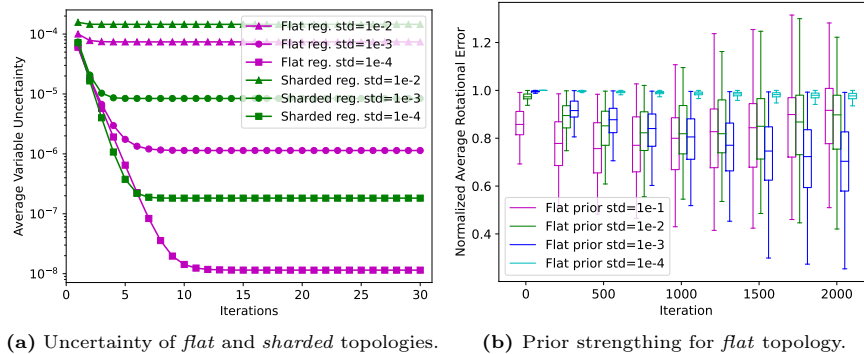


Fig. 5: Analysis of the overconfidence of *flat* topology (left) and its effects on the stability of the system, that can be mitigated by varying prior strength (right).

5.5 Robustness to Noise

The proposed *flat* and *sharded* configurations also handle sensor noise differently. Whereas in previous experiments we have used noise-free images, here we corrupt both images with zero-mean Gaussian noise with standard deviation $\sigma_n = \{0.0, 5 \cdot 10^{-2}, 10^{-1}\}$. We consider two alternative configurations with either weak ($\sigma_R = 10^{-3}$) or strong regularization ($\sigma_R = 10^{-4}$) (other parameters as in Sec. 5.4), with results depicted in Fig. 6a and Fig. 6b, respectively.

While the performance of the system degrades as the level of image noise increases, we observe that the *sharded* topology consistently outperforms the *flat*

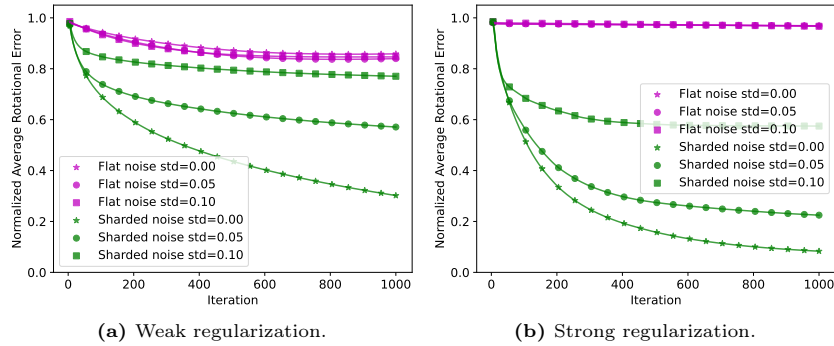


Fig. 6: Performance of the *flat* and *sharded* configuration in the presence of noise employing weak or strong regularization.

one even in the presence of the strongest noise level. Using a stronger regularization factor, however, helps to mitigate such detrimental effects while producing an overall better estimate as discussed in Sec. 5.3. Despite the generally poor performance of the *flat* topology, it is noteworthy that adding noise slightly improves the estimation capabilities of this topology. This behaviour could be explained by interpreting the image noise as a way to disrupt the overconfidence of the synchronous GBP steps, similar to improvement reported when randomly dropping messages [38].

6 Conclusions

This paper presents, to the best of our knowledge, the first approach that decomposes the well-known direct frame-to-frame rotation estimation problem into a pixel-distributed approach, employing only local message-passing between variables. The presented evaluation is not limited to validating the performance of the approach on the rotation estimation task but also provides a more in-depth analysis of the nuances of distributing the global estimation problem at pixel level. In this regard, we believe that the investigation presented in this paper opens up interesting research directions for the future co-design of emerging algorithms and visual sensors with extended computational processing capabilities.

References

1. Albanis, G., Zioulis, N., Drakoulis, P., Gkitsas, V., Sterzentsenko, V., Alvarez, F., Zarpalas, D., Daras, P.: Pano3D: A Holistic Benchmark and a Solid Baseline for 360° Depth Estimation. In: 2021 IEEE/CVF Conference on Computer Vision and Pattern Recognition Workshops (CVPRW). pp. 3722–3732 (Jun 2021). <https://doi.org/10.1109/CVPRW53098.2021.00413> 9
2. Alzugaray, I., Chli, M.: Asynchronous Multi-Hypothesis Tracking of Features with Event Cameras. In: 2019 International Conference on 3D Vision (3DV). pp. 269–278 (Sep 2019). <https://doi.org/10.1109/3DV.2019.00038> 3

3. Alzugaray, I., Chli, M.: HASTE: Multi-Hypothesis Asynchronous Speeded-up Tracking of Events. In: 31st British Machine Vision Virtual Conference (BMVC 2020) (Oct 2020). <https://doi.org/10.3929/ETHZ-B-000439297> 3
4. Asgari, B., Hadidi, R., Shoghi Ghalesahi, N., Kim, H.: PISCES: Power-Aware Implementation of SLAM by Customizing Efficient Sparse Algebra. In: 2020 57th ACM/IEEE Design Automation Conference (DAC). pp. 1–6. IEEE, San Francisco, CA, USA (Jul 2020). <https://doi.org/10.1109/DAC18072.2020.9218550> 3
5. Baker, S., Matthews, I.: Lucas-Kanade 20 Years On: A Unifying Framework. *International Journal of Computer Vision* **56**(3), 221–255 (Feb 2004). <https://doi.org/10.1023/B:VISI.0000011205.11775.fd> 3, 6
6. Baker, S., Scharstein, D., Lewis, J.P., Roth, S., Black, M.J., Szeliski, R.: A Database and Evaluation Methodology for Optical Flow. *International Journal of Computer Vision* **92**(1), 1–31 (Mar 2011). <https://doi.org/10.1007/s11263-010-0390-2> 3
7. Barfoot, T.D.: *State Estimation for Robotics*. Cambridge University Press, 1 edn. (Jul 2017). <https://doi.org/10.1017/9781316671528> 5
8. Bishop, C.M.: *Pattern Recognition and Machine Learning*. Information Science and Statistics, Springer, New York (2006) 2, 3, 4
9. Boikos, K., Bouganis, C.S.: Semi-dense SLAM on an FPGA SoC. In: 2016 26th International Conference on Field Programmable Logic and Applications (FPL). pp. 1–4 (Aug 2016). <https://doi.org/10.1109/FPL.2016.7577365> 3
10. Bose, L., Chen, J., Carey, S.J., Dudek, P., Mayol-Cuevas, W.: Visual Odometry for Pixel Processor Arrays. In: 2017 IEEE International Conference on Computer Vision (ICCV). pp. 4614–4622. IEEE, Venice (Oct 2017). <https://doi.org/10.1109/ICCV.2017.493> 3
11. Bournias, I., Chotin, R., Lacassagne, L.: FPGA Acceleration of the Horn and Schunck Hierarchical Algorithm. In: 2021 IEEE International Symposium on Circuits and Systems (ISCAS). pp. 1–5. IEEE, Daegu, Korea (May 2021). <https://doi.org/10.1109/ISCAS51556.2021.9401068> 3
12. Boyd, S., Parikh, N., Chu, E., Peleato, B., Eckstein, J.: Distributed Optimization and Statistical Learning via the Alternating Direction Method of Multipliers. *Foundations and Trends® in Machine Learning* **3**(1), 1–122 (Jul 2011). <https://doi.org/10.1561/2200000016> 3
13. Campos, C., Elvira, R., Rodríguez, J.J.G., M. Montiel, J.M., D. Tardós, J.: ORB-SLAM3: An Accurate Open-Source Library for Visual, Visual-Inertial, and Multimodal SLAM. *IEEE Transactions on Robotics* pp. 1–17 (2021). <https://doi.org/10.1109/TR0.2021.3075644> 3
14. Carey, S.J., Lopich, A., Barr, D.R.W., Wang, B., Dudek, P.: A 100,000 fps Vision Sensor with Embedded 535GOPS/W 256x256 SIMD Processor Array 3
15. Carey, S.J., Lopich, A., Barr, D.R., Wang, B., Dudek, P.: A 100,000 fps vision sensor with embedded 535GOPS/W 256x256 SIMD processor array. In: 2013 Symposium on VLSI Circuits. pp. C182–C183 (Jun 2013) 2
16. Davison, A.J., Ortiz, J.: FutureMapping 2: Gaussian Belief Propagation for Spatial AI (Oct 2019) 2, 3, 4, 9
17. Davison, A.J., Reid, I.D., Molton, N.D., Stasse, O.: MonoSLAM: Real-Time Single Camera SLAM. *IEEE Transactions on Pattern Analysis and Machine Intelligence* **29**(6), 1052–1067 (Jun 2007). <https://doi.org/10.1109/TPAMI.2007.1049> 3
18. Dellaert, F., Kaess, M.: Factor Graphs for Robot Perception. *Foundations and Trends in Robotics* **6**(1-2), 1–139 (2017). <https://doi.org/10.1561/2300000043> 4

19. Du, J., Ma, S., Wu, Y.C., Kar, S., Moura, J.M.F.: Convergence Analysis of Belief Propagation on Gaussian Graphical Models (Jan 2018) **6**
20. Engel, J., Koltun, V., Cremers, D.: Direct Sparse Odometry. *IEEE Transactions on Pattern Analysis and Machine Intelligence* **40**(3), 611–625 (Mar 2018). <https://doi.org/10.1109/TPAMI.2017.2658577> **3**
21. Engel, J., Schöps, T., Cremers, D.: LSD-SLAM: Large-Scale Direct Monocular SLAM. In: *European Conference on Computer Vision (ECCV)*, vol. 8690, pp. 834–849. Springer International Publishing, Cham (2014). https://doi.org/10.1007/978-3-319-10605-2_54 **3**
22. Eriksson, A., Bastian, J., Chin, T.J., Isaksson, M.: A Consensus-Based Framework for Distributed Bundle Adjustment. In: *2016 IEEE Conference on Computer Vision and Pattern Recognition (CVPR)*. pp. 1754–1762. IEEE, Las Vegas, NV, USA (Jun 2016). <https://doi.org/10.1109/CVPR.2016.194> **3**
23. Fang, W., Zhang, Y., Yu, B., Liu, S.: FPGA-based ORB feature extraction for real-time visual SLAM. In: *2017 International Conference on Field Programmable Technology (ICFPT)*. pp. 275–278 (Dec 2017). <https://doi.org/10.1109/FPT.2017.8280159> **3**
24. Gao, X., Zhu, L., Cui, H., Xie, Z., Shen, S.: IRA++: Distributed Incremental Rotation Averaging. *IEEE Transactions on Circuits and Systems for Video Technology* **32**(7), 4885–4892 (Jul 2022). <https://doi.org/10.1109/TCSVT.2021.3118883> **3**
25. Greatwood, C., Bose, L., Richardson, T., Mayol-Cuevas, W., Chen, J., Carey, S.J., Dudek, P.: Perspective Correcting Visual Odometry for Agile MAVs using a Pixel Processor Array. In: *2018 IEEE/RSJ International Conference on Intelligent Robots and Systems (IROS)*. pp. 987–994. IEEE, Madrid (Oct 2018). <https://doi.org/10.1109/IROS.2018.8594500> **3**
26. Halsted, T., Shorinwa, O., Yu, J., Schwager, M.: A Survey of Distributed Optimization Methods for Multi-Robot Systems (Mar 2021) **3**
27. Hartley, R., Aftab, K., Trunpf, J.: L1 rotation averaging using the Weiszfeld algorithm. In: *CVPR 2011*. pp. 3041–3048. IEEE, Colorado Springs, CO, USA (Jun 2011). <https://doi.org/10.1109/CVPR.2011.5995745> **3**
28. Huynh, D.Q.: Metrics for 3D Rotations: Comparison and Analysis. *Journal of Mathematical Imaging and Vision* **35**(2), 155–164 (Oct 2009). <https://doi.org/10.1007/s10851-009-0161-2> **7**
29. Ihler, A.T., Iii, J.W.F., Willsky, A.S.: Loopy Belief Propagation: Convergence and Effects of Message Errors. *Journal of Machine Learning Research* **6**(31), 905–936 (2005) **6, 13**
30. Ishii, I., Taniguchi, T., Yamamoto, K., Takaki, T.: High-Frame-Rate Optical Flow System. *IEEE Transactions on Circuits and Systems for Video Technology* **22**(1), 105–112 (Jan 2012). <https://doi.org/10.1109/TCSVT.2011.2158340> **3**
31. Johnson, J.K., Bickson, D., Dolev, D.: Fixing Convergence of Gaussian Belief Propagation. In: *2009 IEEE International Symposium on Information Theory*. pp. 1674–1678 (Jun 2009). <https://doi.org/10.1109/ISIT.2009.5205777> **13**
32. Klein, G., Murray, D.: Parallel Tracking and Mapping for Small AR Workspaces. In: *2007 6th IEEE and ACM International Symposium on Mixed and Augmented Reality*. pp. 225–234 (Nov 2007). <https://doi.org/10.1109/ISMAR.2007.4538852> **3**
33. LeCun, Y., Chopra, S., Hadsell, R., Ranzato, M., Huang, F.J.: *A Tutorial on Energy-Based Learning* (2007) **4**
34. Leutenegger, S., Lynen, S., Bosse, M., Siegwart, R., Furgale, P.: Keyframe-based visual-inertial odometry using nonlinear optimization. *The International Journal*

- of Robotics Research **34**(3), 314–334 (Mar 2015). <https://doi.org/10.1177/0278364914554813> **3**
35. Lucas, B.D., Kanade, T.: An iterative image registration technique with an application to stereo vision. In: Proceedings of the 7th International Joint Conference on Artificial Intelligence - Volume 2. pp. 674–679. IJCAI'81, Morgan Kaufmann Publishers Inc., San Francisco, CA, USA (Aug 1981) **3**
 36. McConville, A., Bose, L., Clarke, R., Mayol-Cuevas, W., Chen, J., Greatwood, C., Carey, S., Dudek, P., Richardson, T.: Visual Odometry Using Pixel Processor Arrays for Unmanned Aerial Systems in GPS Denied Environments. *Frontiers in Robotics and AI* **7**, 126 (Sep 2020). <https://doi.org/10.3389/frobt.2020.00126> **3**
 37. Mur-Artal, R., Montiel, J.M.M., Tardós, J.D.: ORB-SLAM: A Versatile and Accurate Monocular SLAM System. *IEEE Transactions on Robotics* **31**(5), 1147–1163 (Oct 2015). <https://doi.org/10.1109/TRO.2015.2463671> **3**
 38. Murai, R., Alzugaray, I., Kelly, P.H.J., Davison, A.J.: Distributed Simultaneous Localisation and Auto-Calibration using Gaussian Belief Propagation. *IEEE Robotics and Automation Letters* **9**(3), 2136–2143 (Mar 2024). <https://doi.org/10.1109/LRA.2024.3352361> **2, 3, 4, 13, 14**
 39. Murai, R., Ortiz, J., Saeedi, S., Kelly, P.H.J., Davison, A.J.: A Robot Web for Distributed Many-Device Localisation (Feb 2022) **2, 3, 4, 13**
 40. Murai, R., Saeedi, S., Kelly, P.H.J.: BIT-VO: Visual Odometry at 300 FPS using Binary Features from the Focal Plane. In: 2020 IEEE/RSJ International Conference on Intelligent Robots and Systems (IROS). pp. 8579–8586. IEEE, Las Vegas, NV, USA (Oct 2020). <https://doi.org/10.1109/IROS45743.2020.9341151> **3**
 41. Murphy, K., Weiss, Y., Jordan, M.I.: Loopy Belief Propagation for Approximate Inference: An Empirical Study (Jan 2013). <https://doi.org/10.48550/arXiv.1301.6725> **6, 9, 13**
 42. Nagata, J., Sekikawa, Y.: Tangentially Elongated Gaussian Belief Propagation for Event-Based Incremental Optical Flow Estimation. In: 2023 IEEE/CVF Conference on Computer Vision and Pattern Recognition (CVPR). pp. 21940–21949. IEEE, Vancouver, BC, Canada (Jun 2023). <https://doi.org/10.1109/CVPR52729.2023.02101> **2, 3**
 43. Ortiz, J., Evans, T., Davison, A.J.: A visual introduction to Gaussian Belief Propagation (Jul 2021) **4, 9**
 44. Ortiz, J., Pupilli, M., Leutenegger, S., Davison, A.J.: Bundle Adjustment on a Graph Processor (Mar 2020) **2, 3**
 45. Park, F.C.: Distance Metrics on the Rigid-Body Motions with Applications to Mechanism Design. *Journal of Mechanical Design* **117**(1), 48–54 (Mar 1995). <https://doi.org/10.1115/1.2826116> **7**
 46. Park, F.C., Ravani, B.: Smooth invariant interpolation of rotations. *ACM Transactions on Graphics* **16**(3), 277–295 (Jul 1997). <https://doi.org/10.1145/256157.256160> **7**
 47. Pearl, J.: Probabilistic Reasoning in Intelligent Systems: Networks of Plausible Inference. Morgan Kaufmann Publishers Inc., San Francisco, CA, USA (Aug 1988) **4**
 48. Qin, S., Liu, Q., Yu, B., Liu, S.: PI-BA Bundle Adjustment Acceleration on Embedded FPGAs with Co-observation Optimization. <https://arxiv.org/abs/1905.02373v1> (May 2019) **3**
 49. Qin, T., Li, P., Shen, S.: VINS-Mono: A Robust and Versatile Monocular Visual-Inertial State Estimator. *IEEE Transactions on Robotics* **34**(4), 1004–1020 (Aug 2018). <https://doi.org/10.1109/TRO.2018.2853729> **3**

50. Scona, R., Matsuki, H., Davison, A.: From Scene Flow to Visual Odometry Through Local and Global Regularisation in Markov Random Fields. *IEEE Robotics and Automation Letters* **7**(2), 4299–4306 (Apr 2022). <https://doi.org/10.1109/LRA.2022.3150859> **2, 3**
51. Solà, J., Deray, J., Atchuthan, D.: A micro Lie theory for state estimation in robotics. In: arXiv (Nov 2020) **5**
52. Tron, R., Vidal, R., Terzis, A.: Distributed pose averaging in camera networks via consensus on SE(3). In: 2008 Second ACM/IEEE International Conference on Distributed Smart Cameras. pp. 1–10. IEEE, Palo Alto, CA, USA (Sep 2008). <https://doi.org/10.1109/ICDSC.2008.4635701> **3**
53. Vemulapati, V., Chen, D.: ORB-based SLAM accelerator on SoC FPGA. <https://arxiv.org/abs/2207.08405v1> (Jul 2022) **3**
54. Weberruss, J., Kleeman, L., Boland, D., Drummond, T.: FPGA acceleration of multilevel ORB feature extraction for computer vision. In: 2017 27th International Conference on Field Programmable Logic and Applications (FPL). pp. 1–8 (Sep 2017). <https://doi.org/10.23919/FPL.2017.8056856> **3**
55. Wei, Z., Lee, D.J., Nelson, B.E.: FPGA-based Real-time Optical Flow Algorithm Design and Implementation. *Journal of Multimedia* **2**(5), 38–45 (Sep 2007). <https://doi.org/10.4304/jmm.2.5.38-45> **3**
56. Xia, F., Zamir, A.R., He, Z., Sax, A., Malik, J., Savarese, S.: Gibson Env: Real-World Perception for Embodied Agents. In: 2018 IEEE/CVF Conference on Computer Vision and Pattern Recognition. pp. 9068–9079 (Jun 2018). <https://doi.org/10.1109/CVPR.2018.00945> **9**
57. Zhang, R., Zhu, S., Fang, T., Quan, L.: Distributed Very Large Scale Bundle Adjustment by Global Camera Consensus. In: 2017 IEEE International Conference on Computer Vision (ICCV). pp. 29–38 (Oct 2017). <https://doi.org/10.1109/ICCV.2017.13> **3**
58. Ziegler, T., Karrer, M., Schmuck, P., Chli, M.: Distributed Formation Estimation Via Pairwise Distance Measurements. *IEEE Robotics and Automation Letters* **6**(2), 3017–3024 (Apr 2021). <https://doi.org/10.1109/LRA.2021.3062347> **3**